Nanoscale

PAPER

View Article Online
View Journal

Cite this: DOI: 10.1039/d1nr07079g

Anisotropic nodal loop in NiB_2 monolayer with nonsymmorphic configuration†

Qian Xia, ‡[a] Yang Hu,‡[a] Ya-ping Wang,[b] Chang-wen Zhang,[a] Miao-juan Ren,[a] Sheng-shi Li *[a] and Wei-xiao Ji *[a]

Received 26th October 2021,
Accepted 22nd December 2021

DOI: 10.1039/d1nr07079g

rsc.li/nanoscale

Two-dimensional (2D) materials featuring a nodal-loop (NL) state have been drawing considerable attention in condensed matter physics and materials science. Owing to their structural polymorphism, recent high-profile metal-boride films have great advantages and the potential to realize a NL. Herein, a 2D NiB_2 monolayer with an anisotropic NL nature is proposed and investigated using first-principles calculations. We show that the NiB_2 monolayer has excellent thermal dynamics stability, suggesting the possibility of its synthesis in experiments. Remarkably, the NL with a considerable Fermi velocity is demonstrated to be protected by nonsymmorphic glide mirror symmetry, instead of the widely known horizontal mirror symmetry. Accompanied by the proper preservation of the NL, strain engineering can not only regulate the anisotropy of the NL but also give rise to a self-doping phenomenon characterized by effective modulation of the carrier type and concentration. Moreover, this NL state is robust against the correlation effect. These findings pave the way for exploring nonsymmorphic-symmetry-enabled NL nature in 2D metal-borides.

1. Introduction

Two-dimensional nodal-loop semimetals (NLSMs),[1–3] which serve as platforms for fundamental physical research and next-generation technological applications, have attracted considerable interest in recent years. Unlike the discrete point in Dirac and Weyl semimetals,[4–7] the band crossing in NLSMs extends continuously and forms a one-dimensional loop in momentum space with crystal symmetry protection, which is expected to induce exotic phenomena, such as drumhead surface states and intriguing transport properties. Various three-dimensional (3D) materials have been theoretically and experimentally demonstrated as candidates for NSLMs.[8–17] In contrast, the exploitation of two-dimensional (2D) NLSMs is more challenging due to the reduction of symmetry operations, and a very limited amount of 2D NLSMs have been predicted, such as Si-Cmma, B_2O, $TaSiTe_6$, *etc.*[18–24] Encouragingly, NL behavior has been verified by experiments in 2D Cu_2Si and CuSe monolayers.[25,26] It is noteworthy that the NL in the above mentioned systems is typically protected by the symmorphic symmetries. Beyond that, nonsymmorphic symmetries, *i.e.*, glide mirror plane,[27–29] have been found to be an alternative protection mechanism for NL, and more importantly, band crossing is inevitable under this circumstance. Consequently, exploring feasible 2D NLSMs with the protection of nonsymmorphic symmetries is urgent and significant, as it promises to promote the development of nanoelectronics.

More recently, various 2D boron allotropes have been fabricated experimentally,[30,31] which has sparked extensive research interest in exploring their exceptional physical properties. However, due to the electron deficiency of the boron atom, the synthesis of 2D boron films (such as borophene) shows an extraordinary dependence on the metal substrate.[32] Another effective strategy in which metal atoms are embedded into the boron framework has also been employed to achieve electron compensation. In this context, a series of new 2D metal-boride monolayers with versatile electronic properties, such as TiB_2,[33] FeB_2,[34] NiB_6,[35] FeB_3,[36] and MnB,[37] have been designed and are predicted to possess a Dirac state or ferromagnetism with a considerable Curie temperature. On the other hand, 2D metal-boride monolayers provide promising platforms for realizing the NL state, since crystal symmetry protection could be available based on their superior structural diversity. Nevertheless, compared with the widely proposed Dirac materials, the NL state in 2D metal-boride monolayers has rarely been reported.

In this work, based on first-principles calculations, we propose a new 2D metal-boride, namely, a NiB_2 monolayer, which possesses an anisotropic NL. The hypercoordinate Ni–B bonds endow the monolayer with superior mechanical strength and dynamic and thermal stabilities. Electronic band

[a]Spintronics Institute, School of Physics and Technology, University of Jinan, Jinan, Shandong 250022, P. R. China. E-mail: sdy_liss@ujn.edu.cn, sps_jiwx@ujn.edu.cn
[b]State Key Lab of Crystal Materials and Institute of Crystal Materials, Shandong University, Jinan, Shandong 250100, P. R. China

†Electronic supplementary information (ESI) available. See DOI: 10.1039/d1nr07079g

‡These authors contributed equally to this work.

calculations reveal that the band crossings that constitute the anisotropic NL are determined by different Ni-d orbital components and have ultrahigh Fermi velocity (v_F). Through symmetry analysis, we find that the NL state is protected by the expected nonsymmorphic glide mirror symmetry, rather than horizontal mirror symmetry, and that it is robust against strain engineering and the correlation effect. Additionally, the strain engineering can effectively modulate the electronic properties of the NiB_2 monolayer by inducing a self-doping effect, which can realize the selective adjustment of the carrier type and concentration. Our results provide new insights into the NL state in 2D metal-borides.

2. Computational details

Our first-principles calculations were performed based on the projector augmented wave (PAW) method,[38] as implemented in the Vienna *ab initio* simulation package (VASP).[39,40] To treat the exchange-correction functional, the generalized gradient approximation (GGA) with Perdew–Burke–Ernzerhof (PBE) realization was adopted,[41,42] and the Hubbard U was applied to address the on-site coulombic interactions of the Ni-d orbitals by setting U_{eff} = 5.1 eV.[43] In addition, a more reliable Heyd–Scuseria–Ernzerhof (HSE06) hybrid functional was employed for the validation of the band structures.[44] The energy cutoff was fixed at 600 eV and a vacuum layer of 20 Å was added to avoid interaction along the c axis. The equilibrium positions of the atoms were calculated *via* structural optimization until the energy and the force converged to less than 10^{-8} eV and 0.0001 eV $Å^{-1}$, respectively. The Brillouin zone (BZ) was sampled by a 17 × 33 × 1 Γ-centered Monkhorst–Pack k-point mesh. The phonon spectrum was calculated based on the density functional perturbation theory (DFPT) method and performed using the Phonopy code.[45] The finite displacement method was used to estimate the elastic matrix elements. The DFT-D3 method was incorporated to describe the interlayer van der Waals interactions for the calculation of the exfoliation energy.[46,47]

3. Results and discussion

Fig. 1(a and b) presents the geometrical structure (top and side views) of the NiB_2 monolayer. This 2D system shows a rectangular lattice, and each unit cell consists of two Ni atoms and four B atoms. This crystal structure belongs to the space group *Pmmn* (D_{2h},[13] no. 59). The optimized lattice parameters were found to be a = 6.025 Å and b = 3.041 Å. It is noteworthy that the NiB_2 monolayer prefers a buckled structure, in which two Ni sublattices are separately located at the upper and lower surface, and the buckling height is 1.04 Å. Each Ni atom is coordinated by six B atoms, forming a hexa-coordination. The Ni–B bond length is found to be 1.96 Å, which is smaller than that of the NiB_6 monolayer,[35] and the B–B bond length (~1.68 Å) is comparable to that in borophene (~1.67 Å),[48] indicating a strong interaction between the Ni atoms and B framework.

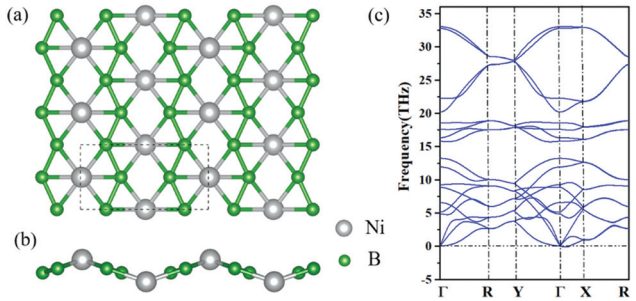

Fig. 1 (a and b) Top and side views of the optimized structure for the NiB_2 monolayer. (c) Calculated phonon dispersion of the NiB_2 monolayer.

To evaluate the stability of the NiB_2 monolayer, we first calculate the cohesive and formation energies, which are defined separately as follows:

$$E_c = (4E_B + 2E_{Ni} - E_{NiB_2})/6$$

$$E_f = (E_{Ni(bulk)} + E_{borophenes} - E_{NiB_2})/6$$

In these formulae, the E_B, E_{Ni}, $E_{Ni(bulk)}$, $E_{borophenes}$ and E_{NiB_2} are the energies of the B atom, Ni atom, bulk Ni unit cell, borphene unit cell and NiB_2 unit cell, respectively. The estimated E_c and E_f are found to be 4.75 eV per atom and 0.14 eV per atom; the former is comparable to that of the FeB_2 monolayer (4.87 eV per atom), and the latter is close to that of $Ni_{23}B_6$ (0.28 eV per atom),[34,49] indicating that the system exhibits favorable stability in terms of energy. The dynamic stability of the monolayer was checked by calculating the phonon spectra. As illustrated in Fig. 1(c), there was no imaginary mode of lattice vibration in the first BZ, which reveals that the NiB_2 monolayer is dynamically stable. More interestingly, compared to that of MoS_2 (14.19 THz),[50] the highest frequency mode of the NiB_2 monolayer has a higher value of 33 THz, implying a robust Ni–B bonding interaction in the system.[51]

Furthermore, to verify that the NiB_2 would be stable under ambient conditions, we performed an *ab initio* molecular dynamics (AIMD) simulation at 300 K using a 3 × 6 supercell. The result shows that the total energy of the NiB_2 monolayer fluctuates smoothly with a specific energy interval after 10 ps of preheating (Fig. 2(a)). From the snapshots in Fig. S1,† one can see that the original crystal structure is well preserved, with no structural reconstruction or lattice collapse. Thus, the NiB_2 monolayer is thermally stable and its structural integrity, along with its symmetry, would be maintained at room temperature to a great extent.

We then focused on the mechanical characteristics of the NiB_2 monolayer, which are important for its potential application. The elastic constants were calculated to be C_{11} = 138.89 N m^{-1}, C_{12} = 68.63 N m^{-1}, C_{22} = 202.73 N m^{-1}, and C_{44} = 77.89 N m^{-1}. These can satisfy Born's criteria[52] well ($C_{11} > 0$, $C_{11}C_{22} > C_{12}^2$, and $C_{44} > 0$). On this basis, the in-plane Young's

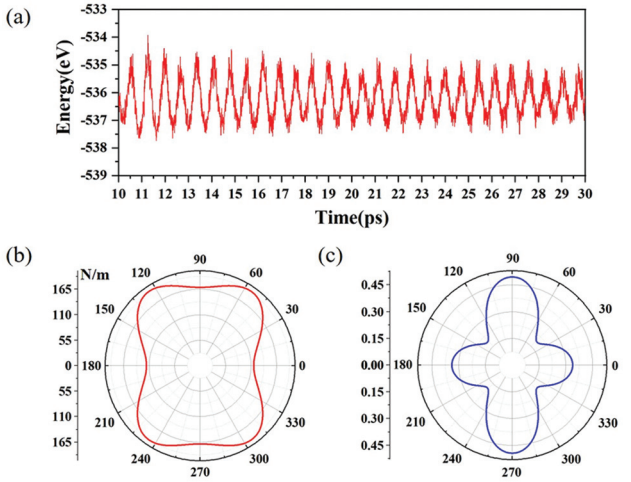

Fig. 2 (a) Variation of total energy for the NiB_2 monolayer at 300 K during the AIMD simulation. (b and c) Young's modulus and Poisson's ratio of the NiB_2 monolayer.

modulus and Poisson's ratio along the arbitrary direction ϕ were calculated using the following formulae:

$$Y(\phi) = \frac{C_{11}C_{22} - {C_{12}}^2}{C_{11}s^4 + C_{22}c^4 + \left(\frac{C_{11}C_{22} - {C_{12}}^2}{C_{44}} - 2C_{12}\right)c^2s^2}$$

$$\nu(\phi) = -\frac{\left(C_{11} + C_{22} - \frac{C_{11}C_{22} - {C_{12}}^2}{C_{44}}\right)c^2s^2 - C_{12}(c^4 + s^4)}{C_{11}s^4 + C_{22}c^4 + \left(\frac{C_{11}C_{22} - {C_{12}}^2}{C_{44}} - 2C_{12}\right)c^2s^2}$$

where $c = \cos\phi$ and $s = \sin\phi$. The corresponding results are plotted in the polar diagrams in Fig. 2(b and c). The in-plane Young's moduli along the *a*-axis and *b*-axis are 115.65 N m^{-1} and 168.80 N m^{-1}, respectively. Note that the minimum value of Young's modulus is still larger than that of silicene (62 N m^{-1}),[53] which would lead to considerable in-plane stiffness and strong bonding between atoms, and the crispation of the NiB_2 monolayer is restrained. The calculated Poisson's ratios are 0.34 along the *a*-axis and 0.49 along the *b*-axis. The orientation-dependent Young's modulus and Poisson's ratio testify to the anisotropic mechanical features in the NiB_2 monolayer.

Next, the electronic properties of the NiB_2 monolayer were investigated. By including the spin polarization in the calculations, we find that the NiB_2 monolayer is nonmagnetic; the corresponding band structure is presented in Fig. 3(a). As can be seen, the conduction and valence bands meet in the vicinity of the Fermi level and form three band-crossing points, which are located at P_1 (0.29, 0.29, 0.000) along Γ–R, P_2 (0.000, 0.348, 0.000) along Γ–Y and P_3 (0.436, 0.000, 0.000) along Γ–X, respectively. By projecting the atomic orbital contributions on the energy bands, one can see that the electronic states near the Fermi level are predominantly contributed by the Ni-d orbitals. More interestingly, every band crossing corresponds to a specific orbital component, as illustrated in Fig. 3(b),

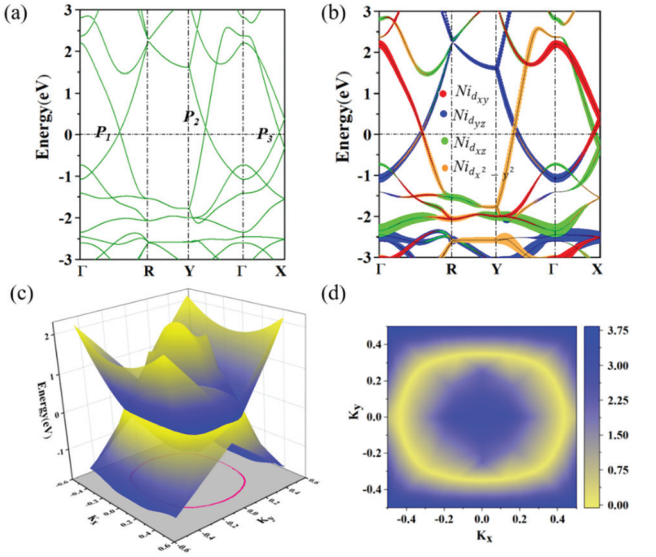

Fig. 3 (a and b) Calculated band structure of the NiB_2 monolayer and corresponding orbital-resolved projection. (c and d) 3D band structure close to the Fermi level and the in-plane projection of the NL.

where crossing points P_1, P_2 and P_3 are dominated by d_{yz}–$d_{x^2y^2}$, d_{yz}–d_{xy} and d_{xy}–d_{xz}, respectively. These band crossings along high-symmetry paths strongly imply the presence of NL nature in the NiB_2 monolayer. To validate this hypothesis, we further plotted the 3D band structure by selecting the energy bands nearest to the Fermi level, as depicted in Fig. 3(c). The plot shows that two energy bands intersect with each other and form a closed NL in the BZ. Fig. 3(d) depicts the in-plane projection of the NL, in which an elliptical loop can be observed intuitively, indicating that the NL has anisotropic characteristics. Furthermore, the linear band crossing would endow the NL with a considerable v_F and massless fermions at the Fermi level. The v_F was checked by fitting the first derivatives of the bands near the NL, *i.e.*, $v_F = \frac{1}{\hbar}\frac{\partial E}{\partial k}$, and the results are listed in Table S1.† We found that the v_F is also direction-dependent, and reaches its highest value of 1.16×10^6 m s^{-1} at the point P_2; this value is comparable to that of graphene (8.2×10^5 m s^{-1}). In addition, based on the expression $m_e^* = \hbar^2/\frac{\partial^2 E}{\partial k^2}$, the effective mass of the electron (m_e^*) at the three band crossings was evaluated, and was found to be very close to zero (see Table S1†), which is conducive to the practical application of the NiB_2 monolayer.

As mentioned above, the existence of a NL requires certain symmetry protection, in which the horizontal mirror symmetry M_z is the most prevalent one. For the NiB_2 monolayer, the space group *Pmmn* contains eight symmetry operators, *i.e.* one identity operator (E), one rotation axis ($C_{2\hat{z}}$), one inversion operator (I), two mirror planes (M_x and M_y), two screw axes ($\left\{C_{2x}\middle|\frac{1}{2}0\right\}$ and $\left\{C_{2y}\middle|0\frac{1}{2}\right\}$) and one glide plane ($\left\{M_z\middle|\frac{1}{2}\frac{1}{2}\right\}$). Obviously, horizontal mirror symmetry M_z can be ruled out as the protec-

tion mechanism, since M_z is intrinsically absent in the NiB_2 monolayer. Using symmetry analysis, we deduced that the NL state in the NiB_2 system is protected by the glide mirror symmetry $\left\{M_z\middle|\frac{1}{2}\frac{1}{2}\right\}$, as illustrated in Fig. S2.† To obtain insight into the protection mechanism, the real-space Kohn–Sham wave functions near the NL are plotted in Fig. S3.† Under the glide mirror operation, we find that the eigenvalues for the hole-like and electron-like band are $+i$ and $-i$, respectively. Consequently, the intersection of these two bands is inevitable and does not involve any hybridization, which gives rise to a gapless NL. Moreover, we calculated the electronic properties of a distorted NiB_2 structure whose glide mirror symmetry was removed by deviating one B atom from its equilibrium position, as shown in Fig. S4.† In this scenario, the NL nature was destroyed due to the band gap opening (274.8 meV, 46.8 meV, and 559.0 meV) at the three band crossings. In short, the glide mirror plays an indispensable role in protecting the NL state in the NiB_2 monolayer.

We further investigated the robustness of the NL state against strain engineering, which is an effective way to modulate the electronic properties of 2D materials. Here, strain engineering was applied by changing the lattice constant, which is defined as $\varepsilon_a = (a - a_0)/a_0$ and $\varepsilon_b = (b - b_0)/b_0$, and the buckled structure of the NiB_2 monolayer is maintained throughout the process. The band structures under three types of strain are presented in Fig. S5–S7,† in which the NL nature is well preserved due to the survival of the glide mirror symmetry, demonstrating the immunity of the NL against strain engineering. Additionally, it is shown that different types of strain engineering play different roles in modulating the electronic properties of the NiB_2 monolayer. For uniaxial strain along the a direction, the tensile strain drives band crossing points P_2 and P_3 to shift above and below the Fermi level, respectively, rendering a self-doping effect featuring p-type and n-type doping along the Γ–Y and Γ–X lines, whereas the opposite phenomenon can be observed for compressive strain. This result is closely correlated with the strain-induced change in buckling height, which would result in an alteration of orbital hybridization and electron distribution. Fig. S8† depicts the partial charge densities at point P_2 under different strains. Electrons on B atoms are transferred to Ni-d orbitals when a compressive strain is applied, thereby leading to n-type doping, while a tensile strain compels the electrons to transfer from Ni to B atoms, and thus p-type doping emerges. On the contrary, moving from compressive strain to tensile strain, the electrons on the Ni atoms undergo a process from dissipation to accumulation, which successively gives rise to p-type and n-type doping at point P_3, as shown in Fig. S9.† More importantly, we find that the strength of the self-doping is enhanced with increasing strain, indicating that the carrier concentration is controllable, while the conversion of p-type and n-type doping *via* strain makes selective carrier doping along a certain direction possible. On the other hand, the uniaxial strain along the b direction mainly adjusts the position of the band crossing point in the BZ. Point P_3 would move towards the high symmetry point X (Γ) under increasing tensile (compressive) strain, which would enlarge (reduce) the anisotropy of the NL. The above two effects can be effectively integrated with the employment of biaxial strain, as illustrated in Fig. S7,† in which simultaneous modulation of the anisotropy of NL and self-doping are achieved. Additionally, the v_F and m_e^* at different band crossings exhibit different responses to strain engineering. For instance, the three types of tensile strain can increase (decrease) the v_F (m_e^*) at points P_1 and P_3 to varying degrees, whereas they have limited influence on point P_2, as listed in Table S1.† In short, strain engineering is an effective route to manipulate the electronic properties of the NiB_2 monolayer without destroying its NL nature.

Considering the fact that electronic properties are generally relevant to the correlation effect of transition metals, we thus checked the band structure of NiB_2 by employing various U_{eff} values, as shown in Fig. 4. When excluding the correlation effect (U_{eff} = 0), there are still three band crossings at high-symmetry lines, indicating that the NL state exists inherently, accompanied by an obvious self-doping phenomenon (Fig. 4(a)). As U_{eff} increases, the NL state is maintained and the intensity of self-doping gradually decreases, which implies a favorable robustness of NL against the correlation effect. Additionally, the NL nature of NiB_2 was further verified using the hybrid HSE06 functional, and the obtained band structure is almost consistent with the result for U_{eff} = 5.1 eV, as shown in Fig. S10(a),† in which the characteristic band crossing can be observed near the Fermi level, indicating the reliability of the NL. The effect of spin–orbit coupling (SOC) on the NL state was also considered. Fig. S10(b)† presents the band structure with SOC taken into account; unfortunately, the three band crossings exhibit different degrees of band gap opening. This is due to the fact that the spin must be explicitly considered when the SOC is included, and thus hybridization becomes inevitable, which would lead to band gap opening at the band crossings. The magnitude of the band gap opening is mainly determined by the SOC strength of the Ni atom, since the electronic states near the Fermi level are dominated by the Ni-d orbitals. In essence, this small band gap opening induced by the SOC would not strictly limit the application of the NiB_2 monolayer at room temperature (26 meV).

In the next section, we analyze the possibility of the experimental synthesis of the NiB_2 monolayer. In view of the fact that atomically 2D boron allotropes have been successfully fabricated, one possible strategy to achieve this goal would be to adsorb Ni atoms on the corresponding boron framework. It is worth mentioning that the hopefully synthesized δ-4 boron layer[48] shows great potential to bond with Ni atoms and form the NiB_2 monolayer. On the other hand, assuming that the bulk form of NiB_2 with a layered structure can be fabricated in the future, like the MXene Mo_2TiC_2,[54,55] the realization of 2D NiB_2 monolayers could be available by the technique of mechanical exfoliation. To employ this approach, it is necessary to determine the interlayer interactions. The exfoliation energy of NiB_2 was then evaluated and found to be 0.257 J

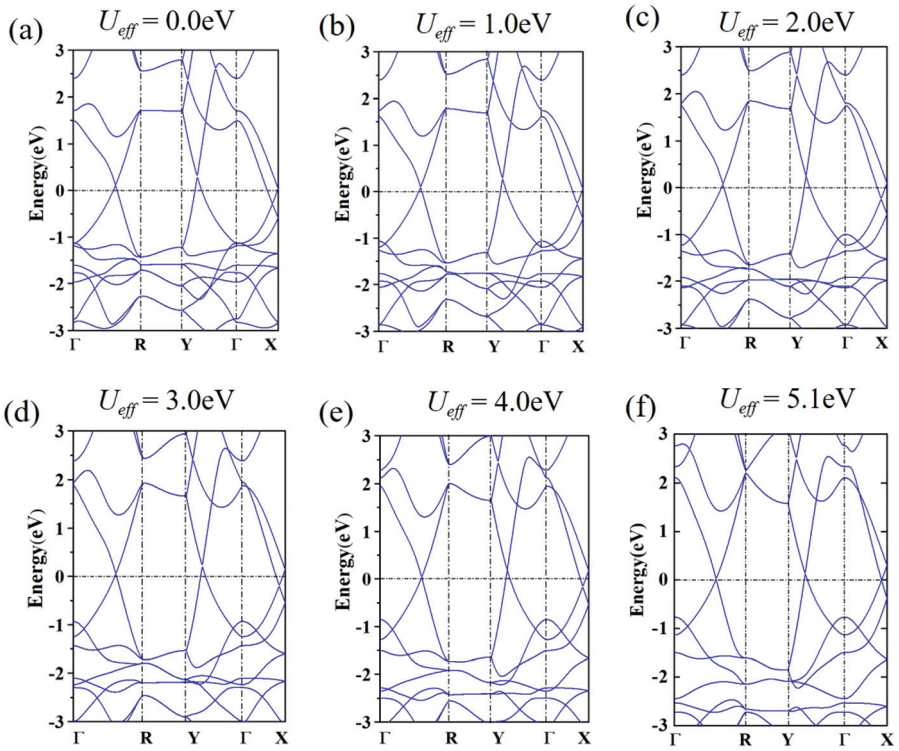

Fig. 4 (a–f) Calculated band structures of the NiB_2 monolayer with different U_{eff} values.

m^{-2}, as shown in Fig. S11.† This value is slightly lower than that of MoS_2,[56] revealing that the experimental mechanical exfoliation of NiB_2 monolayers is feasible.

Having systematically explored the properties of the NiB_2 monolayer, we finally expanded our attention to MB_2 (M = Sc, Ti, V, Cr, Mn, Fe, Co, Cu, Zn) monolayers which share a similar structure to NiB_2. Fig. S12–20† show the corresponding geometric and band structures. We find that only VB_2 and ZnB_2 have a buckled structure, but are still distinguished from the NiB_2 monolayer since the transition metals are located on a plane, while the other systems prefer a planar structure after optimization. Therefore, the selection of transition metal would directly determine the geometric structure of the monolayer, and even the symmetry operation. The magnetic ground states of these monolayers were verified by comparing the energies of nonmagnetic, ferromagnetic and antiferromagnetic configurations, as listed in Table S2.† Additionally, the results of band structure calculations reveal that all the monolayers show metallicity, except for FeB_2, which exhibits semiconducting properties, and unfortunately, the NL characteristics are absent for these systems. Hence, the presence of the NL in the NiB_2 monolayer is due to the joint action of the crystal structure and electron configuration.

4. Conclusion

In summary, we have revealed the NL nature in a NiB_2 monolayer using first-principles calculations, which simultaneously broadens the scope of 2D NL materials and metal-borides. Its favorable dynamic and thermal stabilities suggest that the NiB_2 monolayer has a high potential to be fabricated in experiments. Significantly, the glide mirror symmetry plays a dominant role in protecting the NL in the NiB_2 monolayer, which differs from the horizontal mirror symmetry protection mechanism in other 2D NL materials. The predicted NL state is immune to the correlation effect and strain engineering. More interestingly, strain engineering can give rise to a self-doping phenomenon, where the carrier type and concentration can be manipulated purposefully. Our results provide a desirable platform for exploring the fascinating physics of NLs protected by nonsymmorphic symmetry.

Author contributions

Q. Xia and Y. Hu performed the calculations and data curation and wrote the original draft. Y. Wang and C. Zhang were responsible for supervision. M. Ren participated in the discussion and provided useful suggestions. W. Ji and S. Li conceived the ideas. All authors contributed to the revisions of the manuscript.

Conflicts of interest

The authors declare that they have no conflict of interest.

Acknowledgements

This work was supported by the National Natural Science Foundation of China (Grant no. 12004137, 11804116, 51871112 and 62071200), the Taishan Scholar Project of Shandong Province (ts20190939) and the Natural Science Foundation of Shandong Province (Grant no. ZR2020QA052 and ZR2018MA033).

References

1 Y. Kim, B. J. Wieder, C. L. Kane and A. M. Rappe, *Phys. Rev. Lett.*, 2015, **115**, 036806.
2 K. Mullen, B. Uchoa and D. T. Glatzhofer, *Phys. Rev. Lett.*, 2015, **115**, 026403.
3 A. A. Burkov, M. D. Hook and L. Balents, *Phys. Rev. B: Condens. Matter Mater. Phys.*, 2011, **84**, 235126.
4 S. Borisenko, Q. Gibson, D. Evtushinsky, V. Zabolotnyy, B. Büchner and R. J. Cava, *Phys. Rev. Lett.*, 2014, **113**, 027603.
5 Z. K. Liu, J. Jiang, B. Zhou, Z. J. Wang, Y. Zhang, H. M. Weng, D. Prabhakaran, S. K. Mo, H. Peng, P. Dudin, T. Kim, M. Hoesch, Z. Fang, X. Dai, Z. X. Shen, D. L. Feng, Z. Hussain and Y. L. Chen, *Nat. Mater.*, 2014, **13**, 677–681.
6 Z. K. Liu, B. Zhou, Y. Zhang, Z. J. Wang, H. M. Weng, D. Prabhakaran, S. K. Mo, Z. X. Shen, Z. Fang, X. Dai, Z. Hussain and Y. L. Chen, *Science*, 2014, **343**, 864.
7 B. Q. Lv, N. Xu, H. M. Weng, J. Z. Ma, P. Richard, X. C. Huang, L. X. Zhao, G. F. Chen, C. E. Matt, F. Bisti, V. N. Strocov, J. Mesot, Z. Fang, X. Dai, T. Qian, M. Shi and H. Ding, *Nat. Phys.*, 2015, **11**, 724–727.
8 X. Zhang, Z.-M. Yu, Z. Zhu, W. Wu, S.-S. Wang, X.-L. Sheng and S. A. Yang, *Phys. Rev. B*, 2018, **97**, 235150.
9 R. Yu, H. Weng, Z. Fang, X. Dai and X. Hu, *Phys. Rev. Lett.*, 2015, **115**, 036807.
10 H. Weng, Y. Liang, Q. Xu, R. Yu, Z. Fang, X. Dai and Y. Kawazoe, *Phys. Rev. B: Condens. Matter Mater. Phys.*, 2015, **92**, 045108.
11 Z. Liu, H. Wang, Z. F. Wang, J. Yang and F. Liu, *Phys. Rev. B*, 2018, **97**, 055501.
12 Z. Liu, R. Lou, P. Guo, Q. Wang, S. Sun, C. Li, S. Thirupathaiah, A. Fedorov, D. Shen, K. Liu, H. Lei and S. Wang, *Phys. Rev. X*, 2018, **8**, 031044.
13 H. Huang, K.-H. Jin and F. Liu, *Phys. Rev. B*, 2017, **96**, 115106.
14 L. M. Schoop, M. N. Ali, C. Straßer, A. Topp, A. Varykhalov, D. Marchenko, V. Duppel, S. S. P. Parkin, B. V. Lotsch and C. R. Ast, *Nat. Commun.*, 2016, **7**, 11696.
15 Y. Wu, L.-L. Wang, E. Mun, D. D. Johnson, D. Mou, L. Huang, Y. Lee, S. L. Bud'ko, P. C. Canfield and A. Kaminski, *Nat. Phys.*, 2016, **12**, 667–671.
16 G. Bian, T.-R. Chang, R. Sankar, S.-Y. Xu, H. Zheng, T. Neupert, C.-K. Chiu, S.-M. Huang, G. Chang, I. Belopolski, D. S. Sanchez, M. Neupane, N. Alidoust, C. Liu, B. Wang, C.-C. Lee, H.-T. Jeng, C. Zhang, Z. Yuan, S. Jia, A. Bansil, F. Chou, H. Lin and M. Z. Hasan, *Nat. Commun.*, 2016, **7**, 10556.
17 J. Hu, Z. Tang, J. Liu, X. Liu, Y. Zhu, D. Graf, K. Myhro, S. Tran, C. N. Lau, J. Wei and Z. Mao, *Phys. Rev. Lett.*, 2016, **117**, 016602.
18 Y. Hu, S. S. Li, W. X. Ji, C. W. Zhang, M. Ding, P. J. Wang and S. S. Yan, *J. Phys. Chem. Lett.*, 2020, **11**, 485–491.
19 Y.-J. Jin, R. Wang, J.-Z. Zhao, Y.-P. Du, C.-D. Zheng, L.-Y. Gan, J.-F. Liu, H. Xu and S. Y. Tong, *Nanoscale*, 2017, **9**, 13112–13118.
20 S. Li, Y. Liu, S.-S. Wang, Z.-M. Yu, S. Guan, X.-L. Sheng, Y. Yao and S. A. Yang, *Phys. Rev. B*, 2018, **97**, 045131.
21 S.-S. Wang, Z.-M. Yu, Y. Liu, Y. Jiao, S. Guan, X.-L. Sheng and S. A. Yang, *Phys. Rev. Mater.*, 2019, **3**, 084201.
22 C. Zhong, W. Wu, J. He, G. Ding, Y. Liu, D. Li, S. A. Yang and G. Zhang, *Nanoscale*, 2019, **11**, 2468–2475.
23 N. Zhou, P. Zhou, J. Li, C. He and J. Zhong, *Phys. Rev. B*, 2019, **100**, 115425.
24 P. Zhou, Z. S. Ma and L. Z. Sun, *J. Mater. Chem. C*, 2018, **6**, 1206–1214.
25 B. Feng, B. Fu, S. Kasamatsu, S. Ito, P. Cheng, C. C. Liu, Y. Feng, S. Wu, S. K. Mahatha, P. Sheverdyaeva, P. Moras, M. Arita, O. Sugino, T. C. Chiang, K. Shimada, K. Miyamoto, T. Okuda, K. Wu, L. Chen, Y. Yao and I. Matsuda, *Nat. Commun.*, 2017, **8**, 1007.
26 L. Gao, J. T. Sun, J. C. Lu, H. Li, K. Qian, S. Zhang, Y. Y. Zhang, T. Qian, H. Ding, X. Lin, S. Du and H. J. Gao, *Adv. Mater.*, 2018, **30**, e1707055.
27 J. A. Steinberg, S. M. Young, S. Zaheer, C. L. Kane, E. J. Mele and A. M. Rappe, *Phys. Rev. Lett.*, 2014, **112**, 036403.
28 B.-J. Yang and N. Nagaosa, *Nat. Commun.*, 2014, **5**, 4898.
29 S. M. Young, S. Zaheer, J. C. Y. Teo, C. L. Kane, E. J. Mele and A. M. Rappe, *Phys. Rev. Lett.*, 2012, **108**, 140405.
30 A. J. Mannix, X.-F. Zhou, B. Kiraly, J. D. Wood, D. Alducin, B. D. Myers, X. Liu, B. L. Fisher, U. Santiago, J. R. Guest, M. J. Yacaman, A. Ponce, A. R. Oganov, M. C. Hersam and N. P. Guisinger, *Science*, 2015, **350**, 1513.
31 B. Feng, J. Zhang, Q. Zhong, W. Li, S. Li, H. Li, P. Cheng, S. Meng, L. Chen and K. Wu, *Nat. Chem.*, 2016, **8**, 563–568.
32 Y. Liu, E. S. Penev and B. I. Yakobson, *Angew. Chem., Int. Ed.*, 2013, **52**, 3156–3159.
33 L. Z. Zhang, Z. F. Wang, S. X. Du, H. J. Gao and F. Liu, *Phys. Rev. B: Condens. Matter Mater. Phys.*, 2014, **90**, 161402(R).
34 H. Zhang, Y. Li, J. Hou, A. Du and Z. Chen, *Nano Lett.*, 2016, **16**, 6124–6129.
35 X. Tang, W. Sun, C. Lu, L. Kou and C. Chen, *Phys. Chem. Chem. Phys.*, 2019, **21**, 617–622.
36 C. Tang, K. Ostrikov, S. Sanvito and A. Du, *Nanoscale Horiz.*, 2021, **6**, 43–48.
37 Z. Jiang, P. Wang, X. Jiang and J. Zhao, *Nanoscale Horiz.*, 2018, **3**, 335–341.
38 G. Kresse and D. Joubert, *Phys. Rev. B: Condens. Matter Mater. Phys.*, 1999, **59**, 1758–1775.
39 G. Kresse and J. Furthmüller, *Phys. Rev. B: Condens. Matter Mater. Phys.*, 1996, **54**, 11169–11186.

40 G. Kresse and J. Hafner, *Phys. Rev. B: Condens. Matter Mater. Phys.*, 1994, **49**, 14251–14269.
41 S. Grimme, *J. Comput. Chem.*, 2006, **27**, 1787–1799.
42 J. P. Perdew and Y. Wang, *Phys. Rev. B: Condens. Matter Mater. Phys.*, 1992, **45**, 13244–13249.
43 L. Wang, T. Maxisch and G. Ceder, *Phys. Rev. B: Condens. Matter Mater. Phys.*, 2006, **73**, 195107.
44 J. Paier, M. Marsman, K. Hummer, G. Kresse, I. C. Gerber and J. G. Angyan, *J. Chem. Phys.*, 2006, **124**, 154709.
45 K. Parlinski, Z. Q. Li and Y. Kawazoe, *Phys. Rev. Lett.*, 1997, **78**, 4063–4066.
46 S. Grimme, J. Antony, S. Ehrlich and H. Krieg, *J. Chem. Phys.*, 2010, **132**, 154104.
47 S. Grimme, S. Ehrlich and L. Goerigk, *J. Comput. Chem.*, 2011, **32**, 1456–1465.
48 X. Wu, J. Dai, Y. Zhao, Z. Zhuo, J. Yang and X. C. Zeng, *ACS Nano*, 2012, **6**, 7443–7453.
49 B. Idzikowski and A. Szajek, *J. Optoelectron. Adv. Mater.*, 2003, **5**, 239–244.
50 A. Molina-Sánchez and L. Wirtz, *Phys. Rev. B: Condens. Matter Mater. Phys.*, 2011, **84**, 155413.
51 L. M. Yang, V. Bacic, I. A. Popov, A. I. Boldyrev, T. Heine, T. Frauenheim and E. Ganz, *J. Am. Chem. Soc.*, 2015, **137**, 2757–2762.
52 F. Mouhat and F.-X. Coudert, *Phys. Rev. B: Condens. Matter Mater. Phys.*, 2014, **90**, 224104.
53 Y. Ding and Y. Wang, *J. Phys. Chem. C*, 2013, **117**, 18266–18278.
54 B. Anasori, Y. Xie, M. Beidaghi, J. Lu, B. C. Hosler, L. Hultman, P. R. C. Kent, Y. Gogotsi and M. W. Barsoum, *ACS Nano*, 2015, **9**, 9507–9516.
55 B. Anasori, J. Halim, J. Lu, C. Voigt, L. Hultman and M. Barsoum, *Scr. Mater.*, 2015, **101**, 5–7.
56 T. Björkman, A. Gulans, A. V. Krasheninnikov and R. M. Nieminen, *Phys. Rev. Lett.*, 2012, **108**, 235502.